

Configuration and Evaluation of the WRF Model for the Study of Hawaiian Regional Climate

CHUNXI ZHANG, YUQING WANG, AXEL LAUER, AND KEVIN HAMILTON

International Pacific Research Center, and Department of Meteorology, School of Ocean and Earth Science and Technology, University of Hawaii at Manoa, Honolulu, Hawaii

(Manuscript received 26 September 2011, in final form 30 March 2012)

ABSTRACT

The Weather Research and Forecasting (WRF) model V3.3 has been configured for the Hawaiian Islands as a regional climate model for the region (HRCM). This paper documents the model configuration and presents a preliminary evaluation based on a continuous 1-yr simulation forced by observed boundary conditions with 3-km horizontal grid spacing in the inner nested domain. The simulated vertical structure of the temperature and humidity are compared with twice-daily radiosonde observations at two stations. Generally the trade wind inversion (TWI) height and occurrence days are well represented. The simulation over the islands is compared with observations from nine surface climatological stations and a dense network of precipitation stations. The model simulation has generally small biases in the simulated surface temperature, relative humidity, and wind speed. The model realistically simulated the magnitude and geographical distribution of the mean rainfall over the Hawaiian Islands. In addition, the model simulation reproduced reasonably well the individual heavy rainfall events as seen from the time series of pentad mean rainfall averaged over island scales. Also the model reproduced the geographical variation of the mean diurnal rainfall cycle even though the observed diurnal cycle displays quite different features over different islands. Comparison with results obtained using the land surface dataset from the official release of the WRF model confirmed that the newly implemented land surface dataset generally improved the simulation of surface variables. These results demonstrate that the WRF can be a useful tool for dynamical downscaling of regional climate over the Hawaiian Islands.

1. Introduction

The main Hawaiian Islands stretch between 18.9° and 22.2°N in the central North Pacific and are affected year-round by the prevalent trade winds. The regional climate over the Hawaiian Islands can be characterized by two seasons: “summer” between May and October and “winter” between October and April (http://www.prh.noaa.gov/hnl/pages/climate_summary.php). Despite being in a region of large-scale mean descent, rainfall over the Hawaiian Islands is frequent and abundant principally because of the strong interaction between the orography and prevailing trade winds (Schroeder 1993). The trade wind-induced rainfall along the windward sides of the mountains is the most significant contributor to the statewide rainfall (Lyons 1982). In winter, the trade

winds may be interrupted for days or weeks by the invasion of fronts or migratory cyclones from the midlatitude and by Kona storms (Kona storms are extratropical cyclones usually formed in winter resulting in westerly winds, “Kona” in Hawaiian). Therefore, winter in Hawaii is the season of more frequent heavy rainstorms (Schroeder et al. 1977). In summer, tropical disturbances originating in the intertropical convergence zone (ITCZ) can influence the Hawaiian Islands and occasionally cause severe precipitation events (Chu and Clark 1999). Sometimes, the local sea breeze can also bring heavy showers to the Hawaiian Islands, especially over the Big Island (Schroeder 1981; Chen and Nash 1994). It is a challenge for regional models to simulate all of these different synoptic systems and smaller-scale systems (Fig. 1a), which control the weather and climate in the Hawaiian region. On average about 82% of all days in the Hawaii region are trade wind inversion (TWI) days as defined by Cao et al. (2007), and the trade wind inversion height (Chen and Feng 1995, 2001) and trade wind strength (Esteban and Chen 2008; Carlis et al. 2010)

Corresponding author address: Dr. Yuqing Wang, International Pacific Research Center, SOEST, University of Hawaii at Manoa, 1680 East-West Rd., Honolulu, HI 96822.
E-mail: yuqing@hawaii.edu

have a close relation to precipitation over the Hawaiian Islands. Realistic simulation of trade winds and TWI is critical for any regional climate model (RCM) to be used for dynamical downscaling of the Hawaiian regional climate. In addition, subtropical disturbances (cold fronts and Kona storms) as well as tropical disturbances have to be well represented in a RCM for the region (Chu et al. 1993; Otkin and Martin 2004; Chu and Clark 1999).

The variety of valleys and ridges, broad and steep slopes, gives the Hawaiian Islands a diversity of climates that are quite different from that over the surrounding oceans. The microclimates in the Hawaiian Islands range from humid and tropical windward flanks to dry leeward areas (Giambelluca and Schroeder 1986), hence, a high-resolution numerical model is necessary to resolve the finescale geographical variations. However, increasing resolution is computationally expensive and also requires necessary changes in the representation of model physical processes and even model numerics (Rummukainen 2010). Some previous studies have used 1.5–3-km horizontal grid spacings but mainly for short-term (several days) simulations/forecasts (Zhang et al. 2005a,b; Chen and Feng 2001; Feng and Chen 2001) or at most for summer seasonal forecasts (Nguyen et al. 2010) for the Hawaiian Islands. The short-term integrations by Zhang et al. (2005a) showed that the 1.5-km resolution Mesoscale Spectral Model (MSM) provided better simulation of surface variables than the 10-km model. They also demonstrated that further improvements were achieved by coupling the atmospheric model with a land surface model (LSM).

The Advanced Research Weather Research and Forecasting (WRF-ARW) model has been widely used in dynamical downscaling in recent years (Leung et al. 2006; Bukovsky and Karoly 2009; Zhang et al. 2009; Jiménez et al. 2010). With the increasing capacity of computing facilities, some long-term high-resolution simulations have been attempted recently. For example, Jiménez et al. (2010) performed a 14-yr simulation over complex topography in Spain with 2-km horizontal resolution and showed that the WRF model with high resolution can be used for dynamical downscaling in a region with complex terrain.

Simulation of the trade wind boundary layer regime has been a particular challenge for numerical models (e.g., Wyant et al. 2009; Zhang et al. 2011), but the recent success reported by Zhang et al. (2011) in simulating eastern Pacific climate with a version of WRF-ARW has motivated the present study that will examine how well this model can simulate the small-scale features of the Hawaiian climate. We have configured a nested version of the WRF-ARW model with high resolution to cover the Hawaiian region and implemented

improved land surface specifications for the Hawaiian Islands. We also modified a cloud microphysics scheme in the model to improve the simulation of cloud and precipitation for the region. In this paper we report on a 12-month continuous simulation from October 2005 to November 2006 forced by observed lateral boundary conditions performed with this version of WRF [which we will refer to as the Hawaii Regional Climate Model (HRCM)].

The rest of the paper is organized as follows. In section 2, we describe the configuration of the model and introduce the new land surface dataset we developed for the Hawaiian region and the data used for the verification of our preliminary experiments. Section 3 reports the detailed evaluation of the simulation against available satellite, surface, and radiosonde observations. Particular attention is paid to the evaluation of the precipitation simulated by the high-resolution inner domain 2 (D2). Conclusions are drawn in the last section.

2. Model configuration, datasets, and analysis methods

a. Model configuration

The WRF-ARW version 3.3 (Skamarock et al. 2008) was configured with one-way nesting for two meshes (Fig. 1) of 15- and 3-km horizontal grid spacings, respectively. The model atmosphere is discretized with 31 full terrain-following σ levels in the vertical (14 levels below 700 hPa) with the model top at 10 hPa for both meshes, the same as those used in Zhang et al. (2011). There are 260 grid points in the east–west direction and 320 grid points in the north–south direction for the outer mesh, which is large enough to include both ITCZ and the subtropical region in the central North Pacific. The inner mesh has 276 grid points in the east–west direction and 186 grid points in the north–south direction, which covers the main Hawaiian Islands with enough area for the upstream trade winds in the inner domain. There is a buffer zone with 15 grid points normal to the lateral boundary in the outer domain (D1), which provides the lateral boundary conditions for the inner domain (D2) at every time step.

The WRF Single-Moment 6-Class Microphysics scheme (WSM6) with six prognostic cloud variables is used for grid-scale cloud microphysics processes (Hong and Lim 2006). To better reproduce observed trade wind clouds we replaced the autoconversion and accretion rates in the original WSM6 cloud scheme (Tripoli and Cotton 1980; Hong and Lim 2006) with the parameterizations from Khairoutdinov and Kogan (2000). We found Khairoutdinov and Kogan (2000) performing better

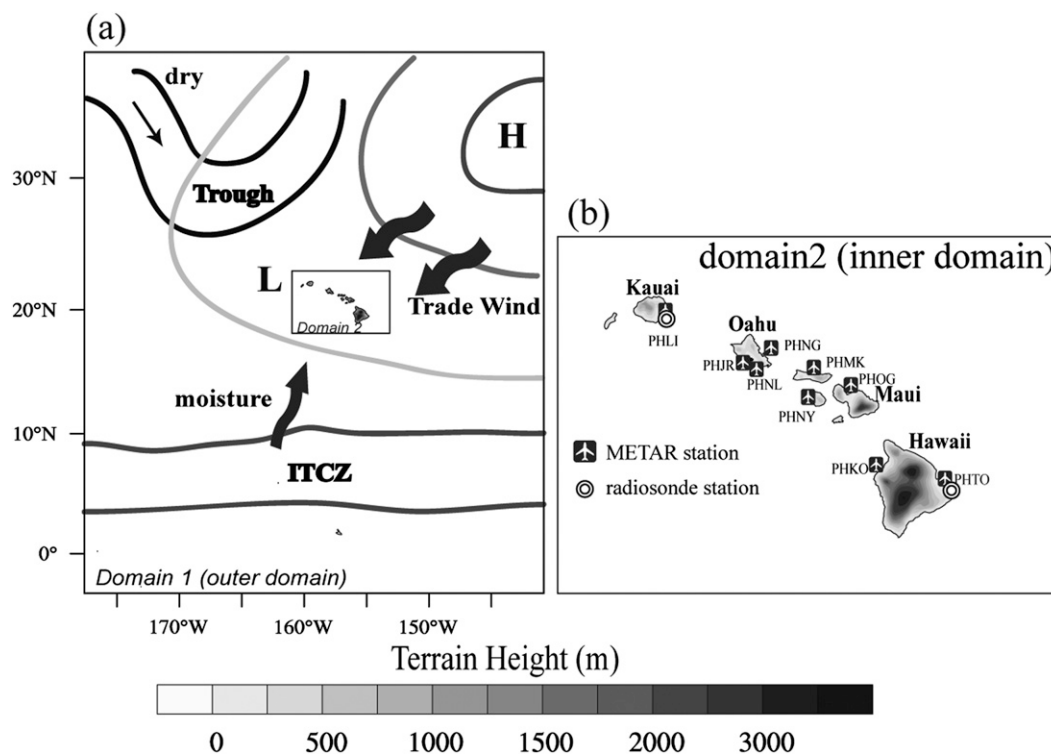


FIG. 1. (a) Model domains and synoptic patterns most relevant to weather and climate in the Hawaiian Islands. (b) The terrain heights and the locations of the METAR stations and radiosonde stations.

particularly in very high-resolution simulations such as in the inner domain D2. In addition, we reduced the cloud droplet number concentration from 300 cm^{-3} in the original code to 55 cm^{-3} , which is more representative for the clean maritime conditions typically found in the Hawaiian region. The shortwave and longwave radiation fluxes are calculated by the Community Atmospheric Model Version 3 radiation scheme (CAM3; Collins et al. 2004). Cloud fraction is diagnosed by grid-scale cloud ice and cloud water mixing ratios and relative humidity (Xu and Randall 1996). We apply the Mellor–Yamada–Janjić planetary boundary layer scheme (MYJ; Janjić 1996, 2002) for the subgrid-scale vertical mixing. The Noah LSM is used for the land surface processes (Chen and Dudhia 2001). We choose the modified Tiedtke scheme (Wang et al. 2003, 2004) for the cumulus parameterization in the outer domain (Zhang et al. 2011). No cumulus parameterization is applied in the inner domain.

The model initial and lateral boundary conditions for the atmosphere were obtained from the Modern-Era Retrospective Analysis for Research and Applications (MERRA) reanalysis from the National Aeronautics and Space Administration (NASA), which covers the satellite era from 1979 to the present and has achieved significant improvements in precipitation and water vapor climatology (Rienecker et al. 2011). The MERRA data have

a horizontal resolution of $0.5^\circ \times 0.6667^\circ$ latitude by longitude and are available at 31 pressure levels from 1000 to 10 hPa at 6-h intervals. The sea surface temperature (SST) is given and updated daily using the $0.25^\circ \times 0.25^\circ$ global analysis provided by National Oceanic and Atmospheric Administration (NOAA; Reynolds et al. 2010). The European Centre for Medium-Range Weather Forecasts (ECMWF) Re-Analysis Interim data (ERA-Interim) provides the initial conditions for soil temperature and moisture (Dee et al. 2011). The diurnal SST variation is calculated based on the surface energy budget with the method from Zeng and Beljaars (2005).

The model was initialized at 0000 UTC 1 October 2005 and integrated continuously until 0000 UTC 1 November 2006. The first month is considered as the model spinup and excluded from further analysis. While soil moisture usually requires a considerably longer spinup period, our analysis showed that the soil moisture for the Hawaiian Islands after the 1-month spinup does not differ too much from the one obtained at the end of the 1-yr simulation. The model evaluation discussed below covers 1 year from 1 November 2005 to 31 October 2006. For the evaluation of the large-scale circulation, two seasons are considered: the winter season from 1 November 2005 to 30 April 2006 and the summer season

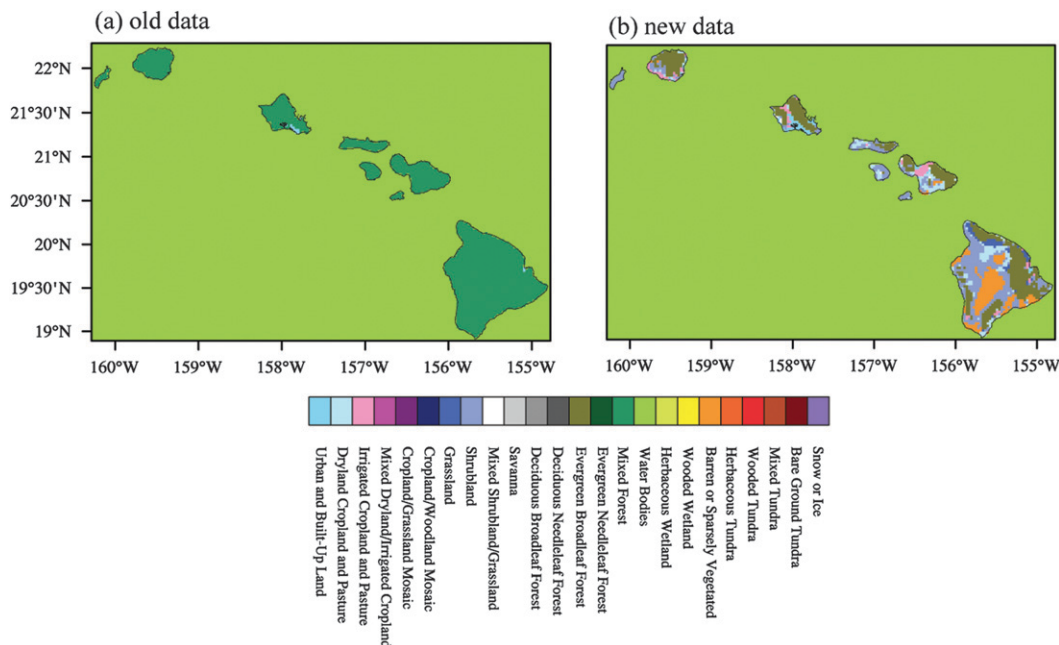


FIG. 2. The (a) old and (b) new land-cover/use data in the Hawaiian region.

from 1 May 2006 to 31 October 2006. This year included an exceptional period of heavy rainfall over much of the main Hawaiian Islands from mid-February to the end of March (<http://www.ncdc.noaa.gov/oa/climate/research/2006/mar/mar06.html>). Two different inner domain runs were conducted with the original land surface data provided by the official WRF release (hereafter OLD) and the new land surface data developed for the Hawaiian region (hereafter NEW, see section 2b) to demonstrate the improvements of the simulation with the new land surface dataset. Note that in both runs, the outer model domain is identical with the new land surface data (e.g., the boundaries for both D2 runs were forced by results from identical D1 integrations by disabling any feedbacks from D2 onto D1).

b. Construction of a new land surface dataset

The land surface properties are fundamental input parameters required for the Noah LSM (Chen and Dudhia 2001). However, the Hawaiian region is not well represented in the land surface datasets of the official WRF model release. These include land cover/use, surface albedo, vegetation types/fraction, and soil types. The poor representations of the land surface properties are mainly caused by the low-resolution datasets (surface albedo, vegetation types/fraction, and soil types) or poorly retrieved datasets (land cover/use) used in the official release of the WRF model for the Hawaiian region. To improve these data, we have implemented the

new land surface properties based on the U.S. Geological Survey (USGS) data and other sources.

The USGS classifies the land surface at each location into one of 24 categories. The official WRF release represents Hawaii by only two of these categories: urban and mixed forests (Fig. 2a). For our new land surface dataset we adapted the publicly available 1-s NLCD (i.e., the 2001 National Land Cover Database; Homer et al. 2004) to match the USGS 24 categories in the Hawaiian region (Fig. 2b). Interpolation is necessary from the 1-s to the HRCM grids. In the NLCD data, there are four types of urban categories based on the density of development. Here, we assigned only the medium and high NLCD urban densities to the urban USGS classification. The National Cooperative Soil Survey superseding the State Soil Geographic datasets (STATSGO) 30-s soil data cover only North America. The global 5-min United Nation Food and Agriculture Organization (FAO) soil data were converted and merged with the North American STATSGO data to composite the 16-category global soil data by the official WRF release (see the WRF manual online at <http://wrf-model.org/index.php>). However the 5-min (around 9 km) resolution is too coarse for our 3-km inner domain (Fig. 3a). The STATSGO spatial and tabulated data were revised and updated in 2006. The STATSGO has been renamed as the U.S. General Soil Map (STATSGO2). We converted the STATSGO2 data in the Hawaiian region to the 16 categories used in WRF model (Fig. 3b).

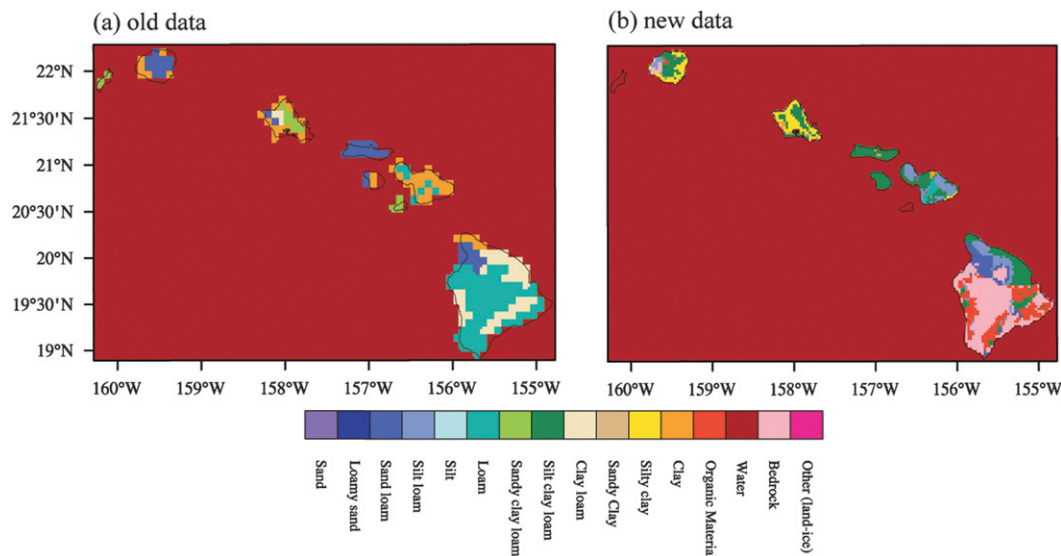


FIG. 3. The (a) old and (b) new top layer soil types in the Hawaiian region.

The old green vegetation fraction (GVF) was derived from the NOAA Advanced Very High Resolution Radiometer (AVHRR) normalized difference vegetation index (NDVI) data and is given by

$$\text{GVF} = (\text{NDVI} - \text{NDVI}_0) / (\text{NDVI}_1 - \text{NDVI}_0), \quad (1)$$

where NDVI_0 (bare soil) and NDVI_1 (dense vegetation) are specified as global constants independent of vegetation/soil type (Gutman and Ignatov 1998). The GVF for the Hawaiian Islands is also only crudely represented in the standard WRF version (Fig. 4a). A 0.05° resolution 5-yr-averaged (2000–04) Moderate Resolution Imaging Spectroradiometer (MODIS) NDVI dataset is used to derive the GVF for the Hawaiian region based on Eq. (1). In our method, NDVI_0 is 0.04, and NDVI_1 is the maximum NDVI in the whole Hawaiian Islands. There are 23 observations at 16-day intervals (viz., the Julian days 001, 017, ..., 353) for each year for the whole dataset. In the end, the derived GVF data are interpolated to monthly data for the WRF (Fig. 4b).

The original surface albedo data in the WRF are derived from measurements of reflected visible and near-infrared radiation by AVHRR on board the NOAA polar-orbiting satellites (Csiszar and Gutman 1999). This dataset, however, does not represent the Hawaiian region well as shown in Fig. 4c. We use 5-yr-averaged (2000–04) MODIS broadband albedo data (collection 4) for visible (VIS; $0.4\text{--}0.7\ \mu\text{m}$) and near infrared (NIR; $0.7\text{--}5.0\ \mu\text{m}$) at 0.05° resolution. As for the NDVI dataset, there are 23 total 16-day intervals (001, 017, ..., 353) for each year for the whole albedo dataset. The MODIS albedo was

generated by a semi-empirical, kernel-driven linear bi-directional reflectance distribution function model (Schaaf et al. 2002). This model relies on the weighted sum of three parameters retrieved from the multivariate multi-angular cloud-free atmosphere with corrected surface reflectance at 1-km resolution, acquired by MODIS during a 16-day period. The MODIS albedo represents the best quality retrieval possible over each 16-day period and consists of local noon black-sky (direct) and white-sky (wholly diffuse) albedo. We evenly averaged both, black-sky and white-sky albedos, as well as the 16-day period albedo to composite a monthly albedo dataset for the WRF (Fig. 4d). Note that some pixels have no data available at all (less than 1%). To resolve this problem, we assign the value based on land-use/cover data to those pixels. As a final step, we also checked the consistency of the albedo with the GVF data.

c. Data for evaluation and analysis methods

In addition to the MERRA reanalysis data mentioned above, more data are used for verification of the model simulations discussed in the following sections. The simulated surface winds are compared with the seasonal surface winds from the Quick Scatterometer (QuikSCAT) measurements over the ocean. The SeaWinds Scatterometer on board the QuikSCAT satellite is a microwave radar launched and operated by the National Aeronautics and Space Administration (NASA). We use monthly mean QuikSCAT data at 25-km resolution provided by the Remote Sensing Systems (http://www.ssmi.com/qscat/qscat_browse.html).

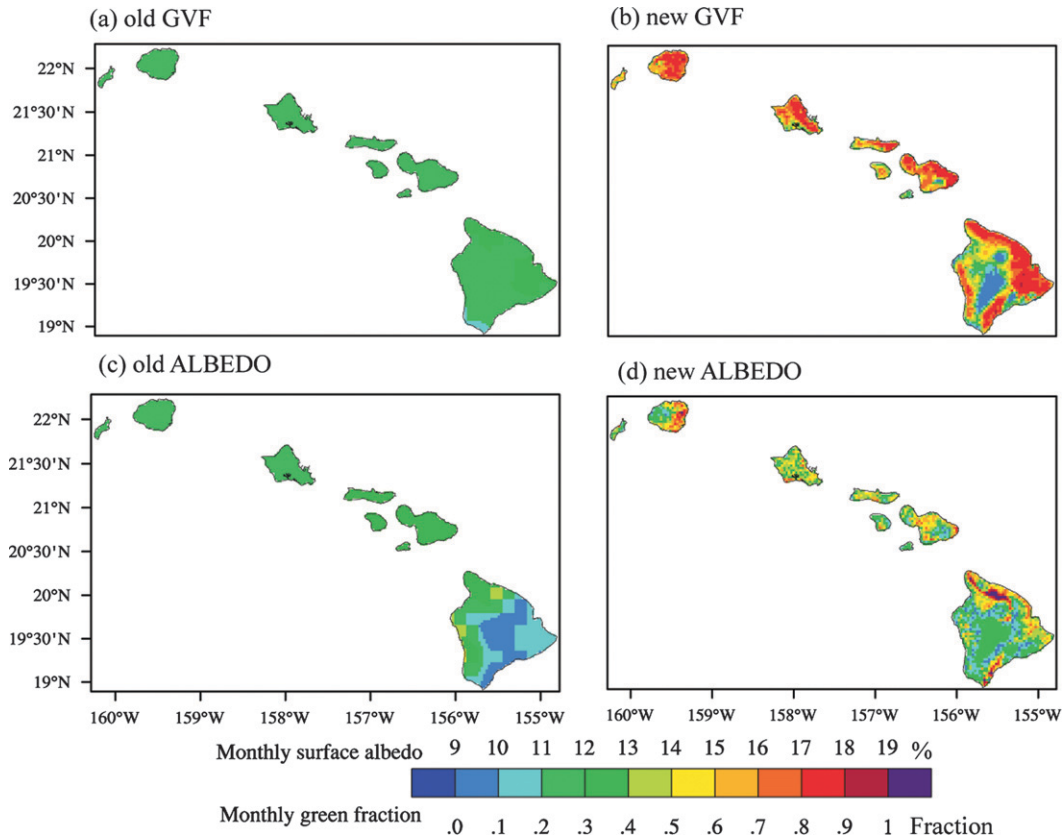


FIG. 4. (a),(b) The old and new monthly green fraction and (c),(d) the monthly surface albedo for January.

The standard “Collection 5.1” MODIS level-3 monthly mean cloud data that have been combined across the *Terra* (morning) and *Aqua* (afternoon) platforms to produce a single dataset with a resolution of $1^\circ \times 1^\circ$ for each month and are available online (<http://climserv.ipsl.polytechnique.fr/cfmip-obs/>). Unlike most other satellite cloud observations, the MODIS algorithm first identifies pixels that are likely to contain clouds. Retrievals of cloud optical depth and cloud particle size are only done for pixels that are likely to be entirely filled with clouds. The first population is summarized in the “mask” estimates of cloud fraction and cloud-top pressure, while the second is summarized in the “retrieval” estimates of cloud fraction and most other variables (Pincus et al. 2012). In our comparison with model results, the retrieval estimates of the total cloud fraction are used, which are obtained closely to the method applied in the model.

There are two sounding stations in the Hawaiian Islands: Lihue (21.97°N, 159.33°W) on the island of Kauai and Hilo (19.72°N, 155.05°W) on the island of Hawaii. Twice-daily (0000 and 1200 UTC) sounding data since 1973 to the present were taken from the University of Wyoming (<http://weather.uwyo.edu/upperair/sounding.html>). The

TWI height is calculated based on the daily observations at 1200 UTC. The algorithm for identifying the inversion follows the method of Guo et al. (2011). We calculated the refractivity N by the relation

$$N = 77.6 \frac{P}{T} + 3.73 \times 10^5 \frac{P_w}{T^2}, \quad (2)$$

where P is the pressure, P_w is the water vapor pressure, and T is the temperature. Both P and P_w are in hectopascals and T is in kelvins. First, we interpolate the retrieved vertical refractivity profiles $N_{(z)}$ to constant vertical intervals (10 m). Second, we apply a linear regression $Az + B$ to $N_{(z)}$ in a sliding window of fixed width of 300 m. The inversion base is in the 300-m range of the window, which has the minimum slope A . Finally, the inversion layer base height is defined as the height at which the maximum lapse of the A calculated from the windows immediately above and below the inversion base. In addition, we require that $|A| > 100 \text{ km}^{-1}$ and that the inversion layer height is in the range 1.0–4.0 km. The slope of the refractivity profile from observational sounding data can reach values as low as -350 km^{-1} in

some cases. Note that because of the fine vertical pressure intervals in observational soundings (less than 5 hPa around the inversion layer height) and the coarse vertical pressure intervals in HRCM (25 hPa around the inversion layer height), we slightly reduced the slope criterion to $|A| > 60 \text{ km}^{-1}$, which is very close to the criterion applied to the Constellation Observing System for Meteorology Ionosphere and Climate (COSMIC) data by Guo et al. (2011), who used $|A| > 50 \text{ km}^{-1}$.

Three surface observational accumulated precipitation datasets for the Hawaiian region are used in our verification of the simulated rainfall. The first dataset is the National Climatic Data Center (NCDC) cooperative monthly precipitation data (<http://www.ncdc.noaa.gov/oa/ncdc.html>), which includes observations from about 190 stations in total. The second dataset is the USGS daily precipitation data (<http://hi.water.usgs.gov/recent/index.html>). The observations at about 30 stations are averaged to get monthly means. Both the NCDC and USGS datasets are quality controlled. The third rainfall dataset is from the Hydronet system, which began collecting 15-min rainfall data in July 1994 (<http://www.prh.noaa.gov/hnl/hydro/hydronet/hydronet-data.php>). Currently the data are collected from 70 rain gauges located throughout the Hawaiian Islands. After a basic

TABLE 1. Names, locations, and elevations of all METAR stations used for the model verification in this study.

Station ID	Station name	Lat (N)	Lon (W)	Elev (m)
PHJR	Oahu, Kalaeloa Airport	21.31°	158.07°	10.0
PHNG	Oahu, Kaneohe Airport	21.45°	157.77°	5.0
PHNL	Oahu, Honolulu International Airport	21.33°	157.94°	3.0
PHTO	Hawaii, Hilo International Airport	19.72°	155.06°	11.0
PHKO	Hawaii, Kailua Kona, Keahole Airport	19.74°	156.05°	13.0
PHLI	Kauai, Lihue Airport	21.98°	159.34°	45.0
PHNY	Lanai, Lanai Airport	20.79°	156.95°	399.0
PHMK	Molokai, Molokai Airport	21.15°	157.10°	138.0
PHOG	Maui, Kahului Airport	20.89°	156.44°	16.0

quality control, we have used data from 65 stations in our study. We converted the 15-min rainfall data to hourly and monthly precipitation values.

We selected observations from nine airports [aviation routine weather report (METAR) Table 1] for verification of the simulated daily mean surface variables.

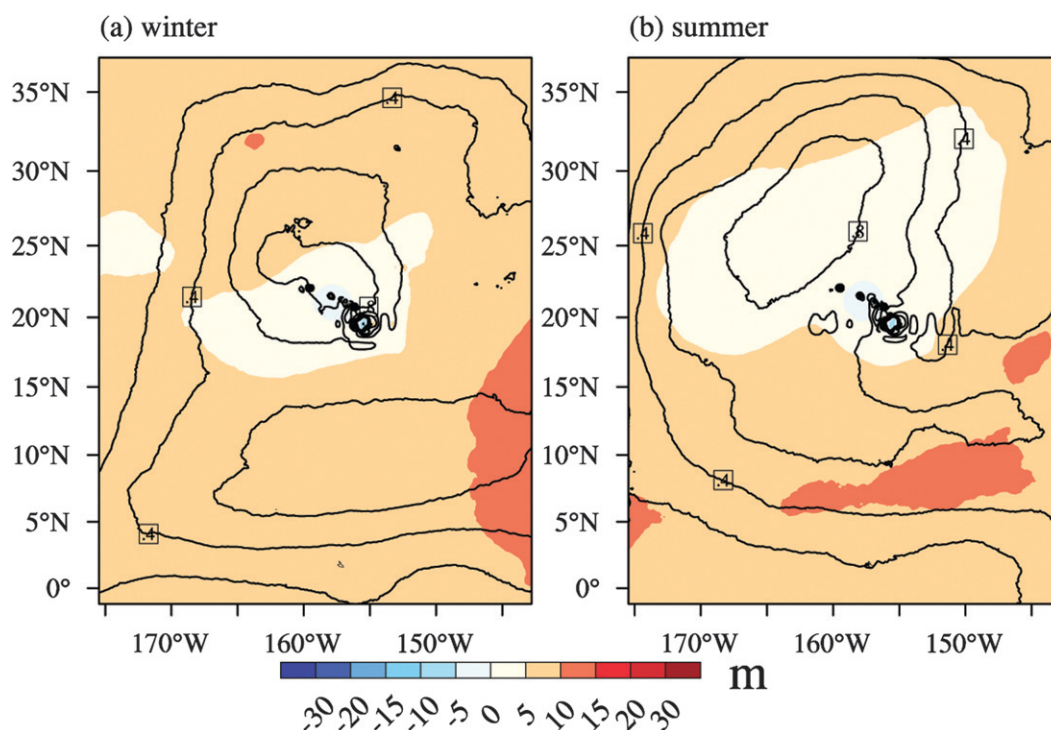


FIG. 5. The biases of the simulated 500-hPa geopotential height (shaded) and mean sea level pressure (contour) in the outer model domain for (a) winter and (b) summer. The contour interval is 0.2 hPa.

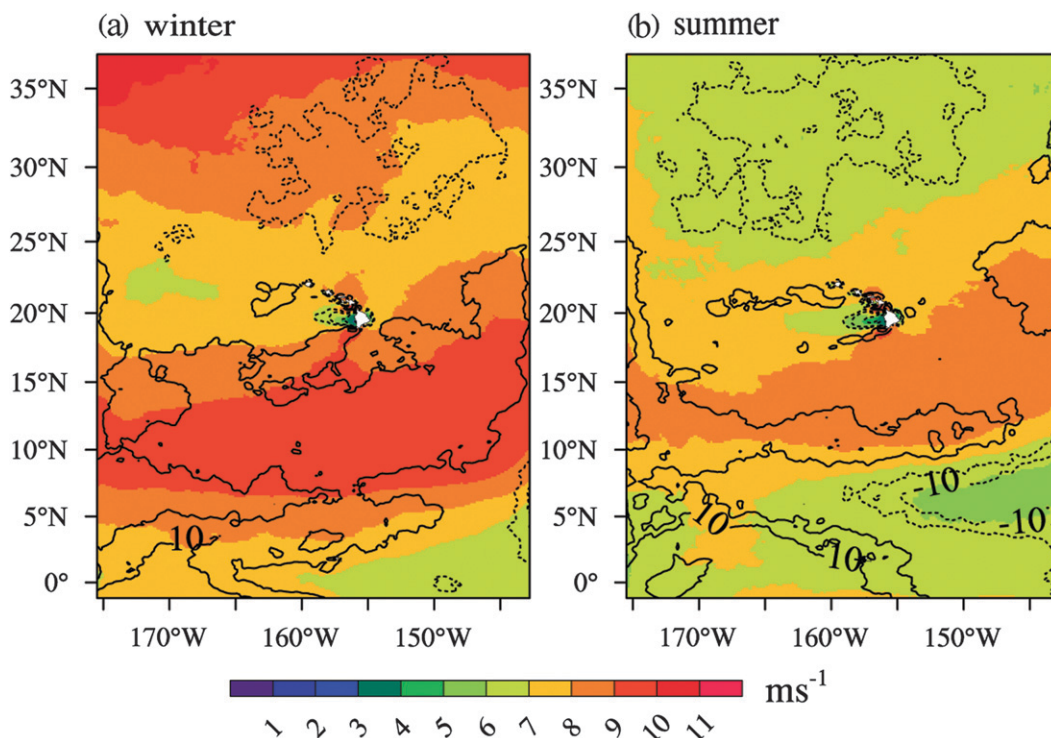


FIG. 6. The simulated surface wind speed (shaded) and its bias ratio (contour, with 5% interval, dashed line is negative bias) for (a) winter and (b) summer in the outer model domain. Observations are from QuikSCAT. The bias ratio is calculated as simulated surface wind speed minus observed wind speed divided by observed wind speed.

Most observed hourly parameters are available from the NCDC website. Note that the METAR observations are taken at around 50th minute of each hour (e.g., 0150, 0250 UTC) but our model output is at 0100, 0200 UTC. The METAR data are quality controlled and averaged to get the daily mean data.

The spatial correlation coefficient between a simulated (m) and an observed (o) quantity a is defined as

$$SC = \frac{\sum_i \sum_j (a_{i,j}^m - \overline{a_{i,j}^m})(a_{i,j}^o - \overline{a_{i,j}^o})}{\left[\sum_i \sum_j (a_{i,j}^m - \overline{a_{i,j}^m})^2 \sum_i \sum_j (a_{i,j}^o - \overline{a_{i,j}^o})^2 \right]^{1/2}}, \quad (3)$$

where subscripts i, j are the horizontal gridpoint indices in the zonal and meridional directions, respectively. The overbar denotes the spatial average over the WRF grids. The temporal correlation coefficient between a simulated (m) and an observed (o) quantity a is defined as

$$R = \frac{\sum_t (a_t^m - \overline{a^m})(a_t^o - \overline{a^o})}{\sqrt{\sum_t (a_t^m - \overline{a^m})^2 \sum_t (a_t^o - \overline{a^o})^2}}, \quad (4)$$

where the subscript t is the given time, and the overbar denotes the time average.

3. Verification of model simulations

The one-way nesting adopted here means that there is no feedback from the inner high-resolution domain onto the outer domain. The outer domain (15 km, D1) offers the inner domain (3 km, D2) lateral boundary conditions at every outer domain time step. As a result, the coarse “outer domain (D1)” simulation is indeed independent of a fine-resolution “inner domain (D2)” simulation. We therefore evaluate the simulations from both domains below.

a. Large-scale circulation

Here we compare the summer- and winter-averaged large-scale circulations from the HRCM simulation with available observations. We focus on the evaluation of the D1 simulation in this and next subsections. The 500-hPa geopotential height (GHT) and mean sea level pressure (MSLP) biases are shown in Fig. 5, which are calculated as the difference between the HRCM simulation and MERRA reanalysis. In both winter and summer, the GHT bias in most of the domain is less than 10 m and even less than 5 m around the Hawaiian Islands. The bias pattern is similar in summer and winter. The positive bias in MSLP is centered around the Hawaiian

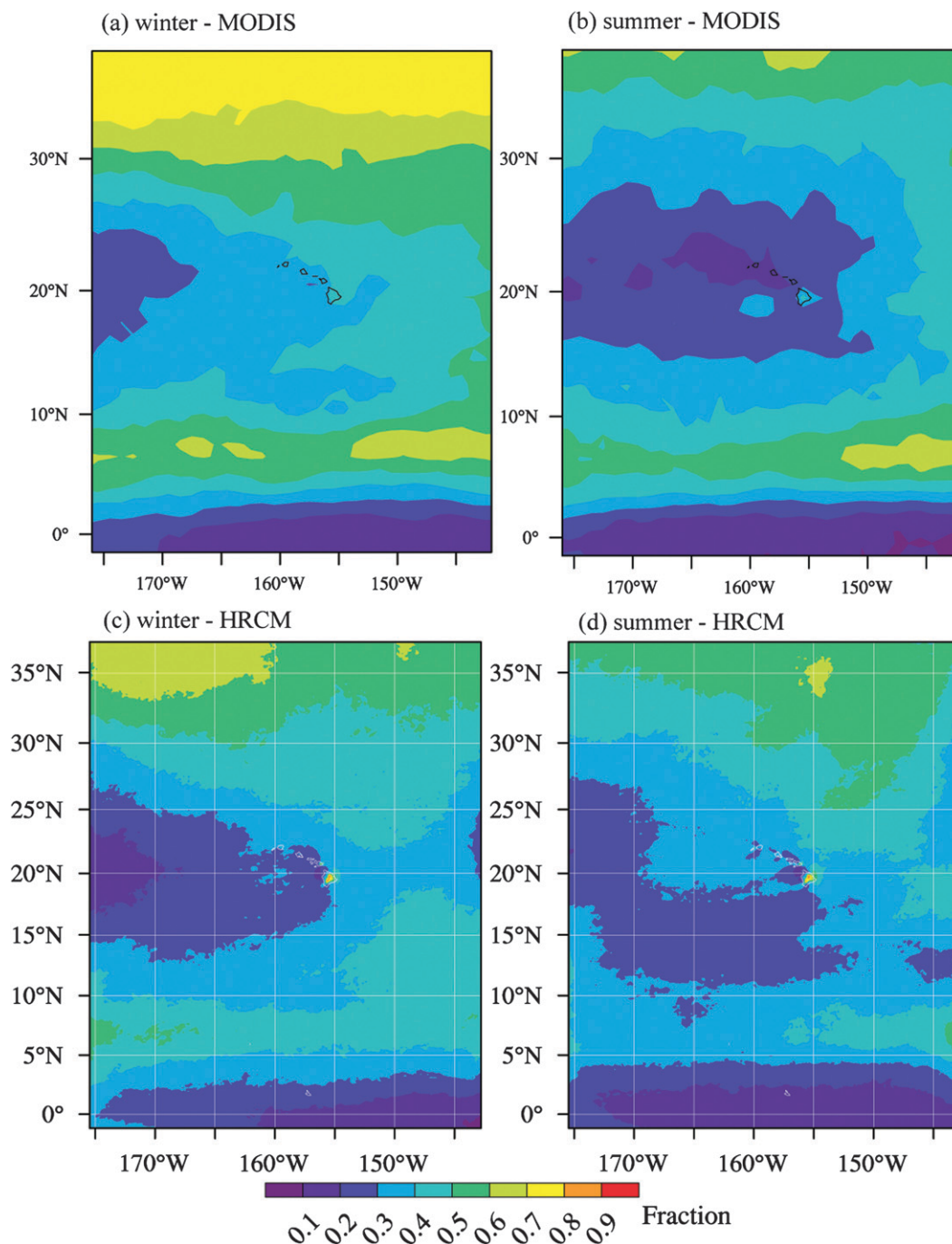


FIG. 7. MODIS-retrieved and model-simulated total cloud fraction for (a),(c) winter and (b),(d) summer.

Islands in winter, while the positive MSLP bias is centered northwest of the Hawaiian Islands in summer. In both seasons, the maximum MSLP biases are less than 1 hPa.

Figure 6 shows the HRCM simulated 10-m height wind speed, which is seasonally averaged. We define the bias in the seasonal mean 10-m height wind speed as the difference between the simulated and the observed

seasonal mean surface wind speed from QuikSCAT. The bias ratio is defined as the bias divided by the QuikSCAT surface wind speed. The observed surface wind speed around the Hawaiian Islands is between 6 and 10 m s^{-1} in winter and about 1 m s^{-1} weaker between 5° and 25°N in summer. The wind speed bias ratio around the Hawaiian Islands in both winter and summer

are generally less than 5% with the actual bias less than about 0.5 m s^{-1} . The negative bias north of the Hawaiian Islands and the positive bias south of the Hawaiian Islands are generally larger, but less than 15%.

Both the simulated and the MODIS-retrieved total cloud fractions for both summer and winter are shown in Fig. 7. The spatial correlation (SC) between the simulated and the MODIS cloud fractions is 0.74 in winter and 0.75 in summer. In winter, the simulated total cloud fraction is about 10%–20% less than that observed in most of domain D1. In summer, the simulated total cloud fraction north of 15°N is close or about 10% higher than that observed. As in winter, the model also underestimates the total cloud fraction in the ITCZ in summer. The MODIS-retrieved total cloud fraction around the Hawaiian Islands in summer (except for the island of Hawaii) is generally less than 10%, but the HRCM-simulated total cloud fraction is between 0.2 and 0.4. Note that MODIS cannot resolve the trade cumuli well commonly found in the Hawaiian region due to its coarse spatial resolution and the thresholds used in the retrieval algorithm (Pincus et al. 2012). Nevertheless, the above comparison still gives some confidence that the HRCM has promising skills in reproducing the cloud distribution at the large scale around the Hawaiian Islands.

b. Vertical structure

One of the main features of the trade wind region is the TWI, which is highly correlated with precipitation at Hilo with a correlation coefficient of greater than 0.7 (Chen and Feng 1995). Figure 8 shows the HRCM simulated and the observed TWI at the two Hawaiian sounding sites (Hilo and Lihue). At Lihue 283 days with the TWI as defined by Guo et al. (2011) were observed at 1200 UTC between 1 November 2005 and 31 October 2006 (76% frequency of occurrence), which is very close to the 82% occurrence frequency for the 25-yr average by Cao et al. (2007) with a different algorithm to detect the TWI height. There are 262 and 283 days found in the model simulation in D1 and D2, respectively. The mean TWI height at Lihue in D1 is 2411 m, about 400 m higher than that determined from the observed soundings at Lihue. In the inner domain D2 the mean TWI height at Lihue is only about 175 m higher than in the observations. At the location of Hilo, the D1 simulates 303 TWI days, which is close to the observed 291 TWI days. The simulated mean TWI height of 2499 m is about 300 m higher than the observed. While there are 327 TWI days at Hilo in D2, and the simulated mean TWI height is about 8 m higher than the observed. In some days, the simulated TWI height in D2 is slightly lower than the observed as seen from Fig. 8.

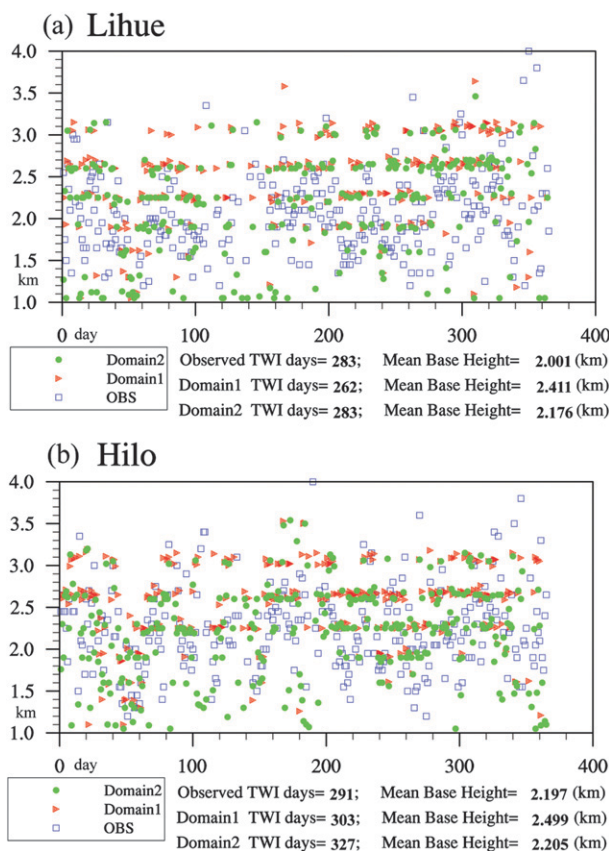


FIG. 8. The observed and the HRCM-simulated TWI days and heights for (a) Lihue, Kauai, and (b) Hilo, Hawaii.

We used the observed soundings at Lihue and Hilo to evaluate the vertical structure of the model atmosphere associated with the TWI. We composited the vertical profiles on TWI days only (as determined by the observed soundings when there is a TWI at Hilo or Lihue) between 1 November 2005 and 31 October 2006. To account for a possible horizontal drift of the balloon in the observations, we averaged the model output over $0.5^\circ \times 0.5^\circ$ grid boxes centered at Lihue and Hilo. Figure 9 shows the vertical profiles of specific humidity and potential temperature from the HRCM simulation, from the observed soundings, and from the MERRA reanalysis, at Lihue and Hilo. The MERRA reanalysis reproduces the observed vertical profile of specific humidity at Lihue except for a small dry bias below 800 hPa and a small wet bias between 600 and 800 hPa (Fig. 9a). The vertical profile of specific humidity in D2 is closer to the observations than that in D1, but there is a wet bias between 850 and 650 hPa in both domains (Fig. 9a). At Lihue, the dry and wet biases in D2 are less than 1.2 g kg^{-1} , but can be as large as 2 g kg^{-1} in D1. A cold bias of 0–3 K between 900 and 650 hPa in the HRCM simulation is present in both D1 and D2. The MERRA reanalysis at

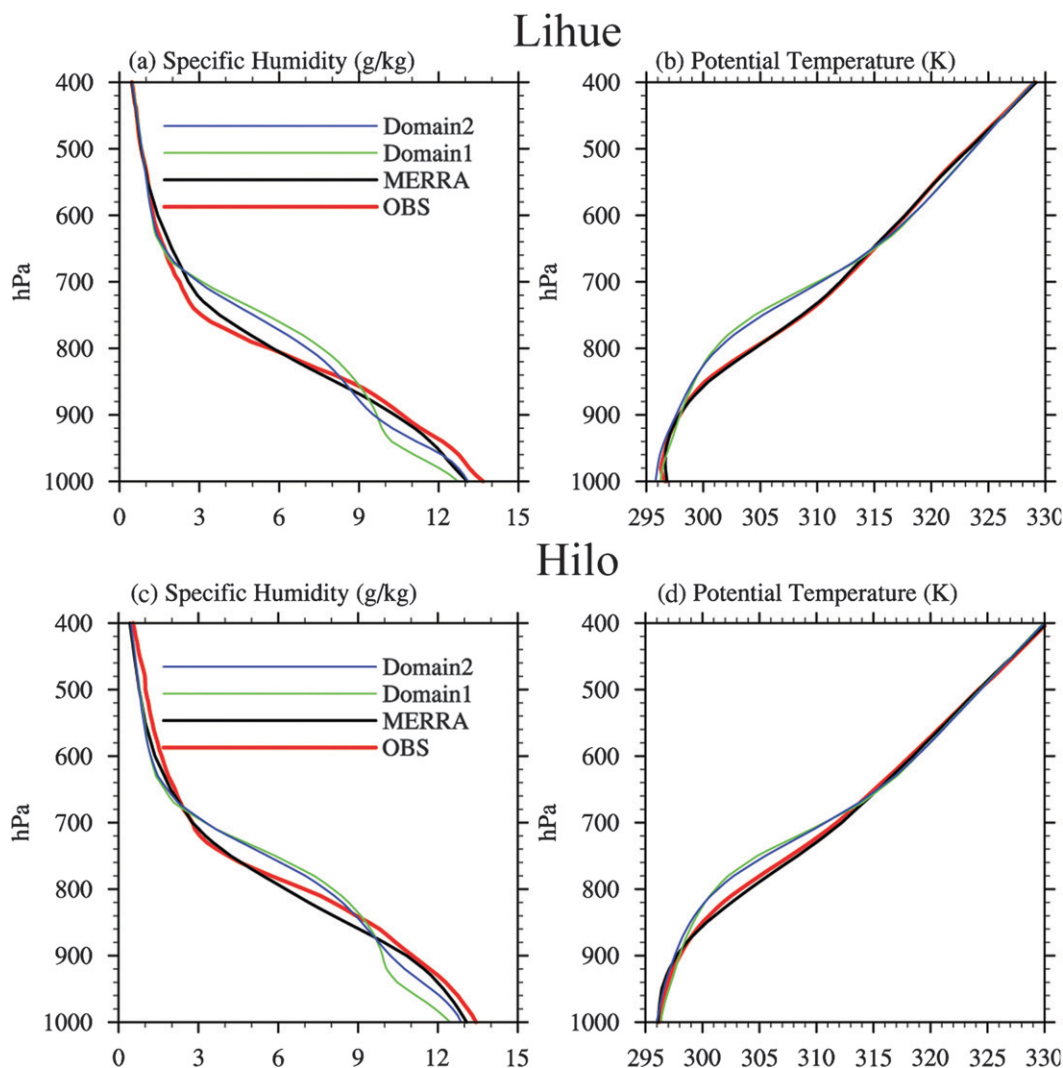


FIG. 9. Vertical profiles of (a),(c) specific humidity and (b),(d) potential temperature averaged over TWI days at (top) Lihue and (bottom) Hilo. Shown are observations (OBS), MERRA reanalysis data, and results for model domains 1 and 2.

Hilo shows a dry bias of $0\text{--}1\text{ g kg}^{-1}$ below 750 hPa compared to the sounding data (Fig. 9c) and a slight warm bias in potential temperature between 850 and 700 hPa (Fig. 9d). In general, the bias from HRCM simulation at Hilo is qualitatively similar to that at Lihue. The HRCM simulates a deep mixed layer in good agreement with the observation. This realistic simulation can be attributed to the use of both the MYJ PBL scheme and the Tiedtke cumulus parameterization (Zhang et al. 2011).

c. Surface variables and influence of the new land surface data

1) DAILY MEAN BIAS OF SURFACE VARIABLES

The HRCM surface hourly outputs are interpolated to the METAR observational stations by using a bilinear

interpolation method. Both the HRCM hourly data and METAR hourly observational data are averaged to calculate the daily mean surface variables including 2-m air temperature, 2-m relative humidity, and 10-m winds. Table 2 shows the statistics of model errors for these variables in the period from 1 November 2005 through 31 October 2006. The root-mean-square errors (RMSE) and mean biases for surface air temperature vary from 0.70 to 1.13 K and from -1.10 to 0.67 K, respectively, among different stations. The magnitude of both RMSE and bias are comparable with those of Nguyen et al. (2010) for the island of Oahu and Yang et al. (2005) for the island of Hawaii. The temporal correlation coefficient for surface air temperature varies between 0.80 and 0.90. Surface relative humidity at all stations is generally well simulated. The temporal correlation coefficient

TABLE 2. RMSE, mean bias (BIAS), and temporal correlation coefficient (R) for the surface variables 2-m air temperature (T), 2-m relative humidity (RH), and 10-m wind speed (WSP). Both the simulation with the new land surface dataset (NEW) and the old land surface dataset (OLD) are presented.

Station ID	T (K)						RH (%)						WSP (m s^{-1})					
	RMSE		BIAS		R		RMSE		BIAS		R		RMSE		BIAS		R	
	OLD	NEW	OLD	NEW	OLD	NEW	OLD	NEW	OLD	NEW	OLD	NEW	OLD	NEW	OLD	NEW	OLD	NEW
PHNL	0.78	0.60	-0.52	-0.12	0.90	0.91	6.85	5.75	4.60	2.55	0.65	0.66	1.04	1.00	0.22	0.35	0.79	0.80
PHTO	0.92	0.83	0.67	0.52	0.84	0.84	8.12	8.03	-6.49	-7.67	0.42	0.51	1.06	1.03	-0.87	-0.87	0.40	0.41
PHKO	1.13	1.01	-1.10	-1.08	0.86	0.86	6.23	5.81	4.10	3.39	0.41	0.43	1.99	1.66	-1.94	-1.56	0.52	0.52
PHLI	0.76	0.63	-0.44	-0.13	0.86	0.86	7.54	7.49	6.82	7.90	0.60	0.56	1.13	1.13	-0.66	-0.54	0.80	0.79
PHNY	0.83	0.80	-0.42	-0.38	0.82	0.84	7.66	7.48	3.66	5.00	0.54	0.52	1.81	2.34	0.96	1.83	0.74	0.74
PHMK	0.77	0.70	-0.36	-0.21	0.81	0.83	5.39	5.31	1.87	2.40	0.44	0.43	1.61	1.99	1.13	1.80	0.81	0.81
PHOG	0.83	0.80	-0.34	-0.29	0.80	0.80	5.12	5.37	-0.90	-1.85	0.49	0.55	1.15	1.05	-0.26	0.58	0.77	0.76
PHJR	0.70	0.65	-0.18	0.13	0.87	0.87	7.38	6.60	3.60	1.78	0.61	0.63	2.46	2.27	1.96	1.39	0.49	0.49
PHNG	0.82	0.75	-0.65	-0.53	0.90	0.90	8.30	7.76	7.78	7.08	0.57	0.55	2.68	2.47	2.54	2.64	0.78	0.78
ALL	0.84	0.75	-0.37	-0.23	0.85	0.86	6.95	6.62	2.78	2.29	0.54	0.55	1.66	1.67	0.34	0.63	0.68	0.68

is between 0.41 and 0.65. However, the model has the biggest difficulty in reproducing the observed surface wind speed. The RMSE of surface wind speed at almost all stations is between 1.0 and 2.7 m s^{-1} , but the bias is much smaller for the average over all stations. Both, the RMSE and the bias of surface wind speed, are the largest at Kaneohe (PHNG) on the island of Oahu. The model does not capture the observed variation of the daily mean surface wind speed at the island of Hawaii. The temporal correlation coefficients are low at Hilo (PHTO) and Kona (PHKO).

The simulation with the new land surface dataset shows an overall improvement in surface air temperature and surface relative humidity compared to that with the old land surface dataset, except for Kahului airport (PHOG) on Maui. The RMSE at the Honolulu Airport (PHNL) is reduced from 0.78 to 0.60, with a cold bias of 0.12 K in the simulation with the new land surface dataset instead of a cold bias of 0.52 K with the old land

surface dataset. The new land surface dataset also improves the simulation of surface relative humidity and surface wind speed at most of the stations. However, the model results with the new land surface dataset do not show improvements at all stations. For example, the RMSE and bias for the simulated surface wind speed at Lanai Airport (PHNY) and Molokai Airport (PHMK) increased in the simulation with the new land surface dataset. Nevertheless, we find an overall improvement in the simulated surface variables using the new land surface dataset.

The surface daily maximum (Tmax) and minimum (Tmin) 2-m temperatures are also compared with observations in this study (Table 3). The nine-station average RMSE for Tmax is 1.39 and 1.25 K, respectively, for the simulations with the old and the new land surface datasets. And the averaged RMSE for Tmin is 1.44 and 1.43 K. The averaged bias and temporal correlation are slightly improved by the new land surface

TABLE 3. RMSE, mean bias (BIAS), and temporal correlation coefficient (R) for the daily maximum and minimum 2-m temperature (K). Both the simulation with the new land surface dataset (NEW) and the old land surface dataset (OLD) are presented.

Station ID	Tmax (K)						Tmin (K)					
	RMSE		BIAS		R		RMSE		BIAS		R	
	OLD	NEW	OLD	NEW	OLD	NEW	OLD	NEW	OLD	NEW	OLD	NEW
PHNL	0.90	0.83	-0.52	-0.58	0.86	0.88	1.36	1.24	-0.20	0.41	0.70	0.75
PHTO	1.09	1.01	-0.58	-0.51	0.73	0.75	1.87	1.72	1.78	1.60	0.66	0.66
PHKO	1.64	1.61	-1.62	-1.55	0.68	0.69	0.88	0.85	-0.05	-0.23	0.68	0.72
PHLI	1.94	1.97	-1.88	-1.91	0.78	0.76	1.35	1.27	0.82	0.41	0.63	0.64
PHNY	1.29	1.27	-0.91	-0.77	0.71	0.75	1.42	1.25	0.93	0.52	0.61	0.62
PHMK	1.11	0.98	-0.75	-0.45	0.78	0.80	1.63	1.56	0.55	0.20	0.51	0.57
PHOG	1.24	1.10	-0.99	-1.19	0.78	0.79	1.85	1.95	0.97	1.42	0.49	0.52
PHJR	1.25	1.39	-1.04	-1.23	0.83	0.84	1.53	1.93	1.02	0.93	0.64	0.67
PHNG	2.04	2.05	-2.00	-2.00	0.80	0.82	1.04	1.07	0.39	0.62	0.67	0.67
ALL	1.39	1.25	-1.14	-1.13	0.77	0.79	1.44	1.43	0.69	0.65	0.62	0.65

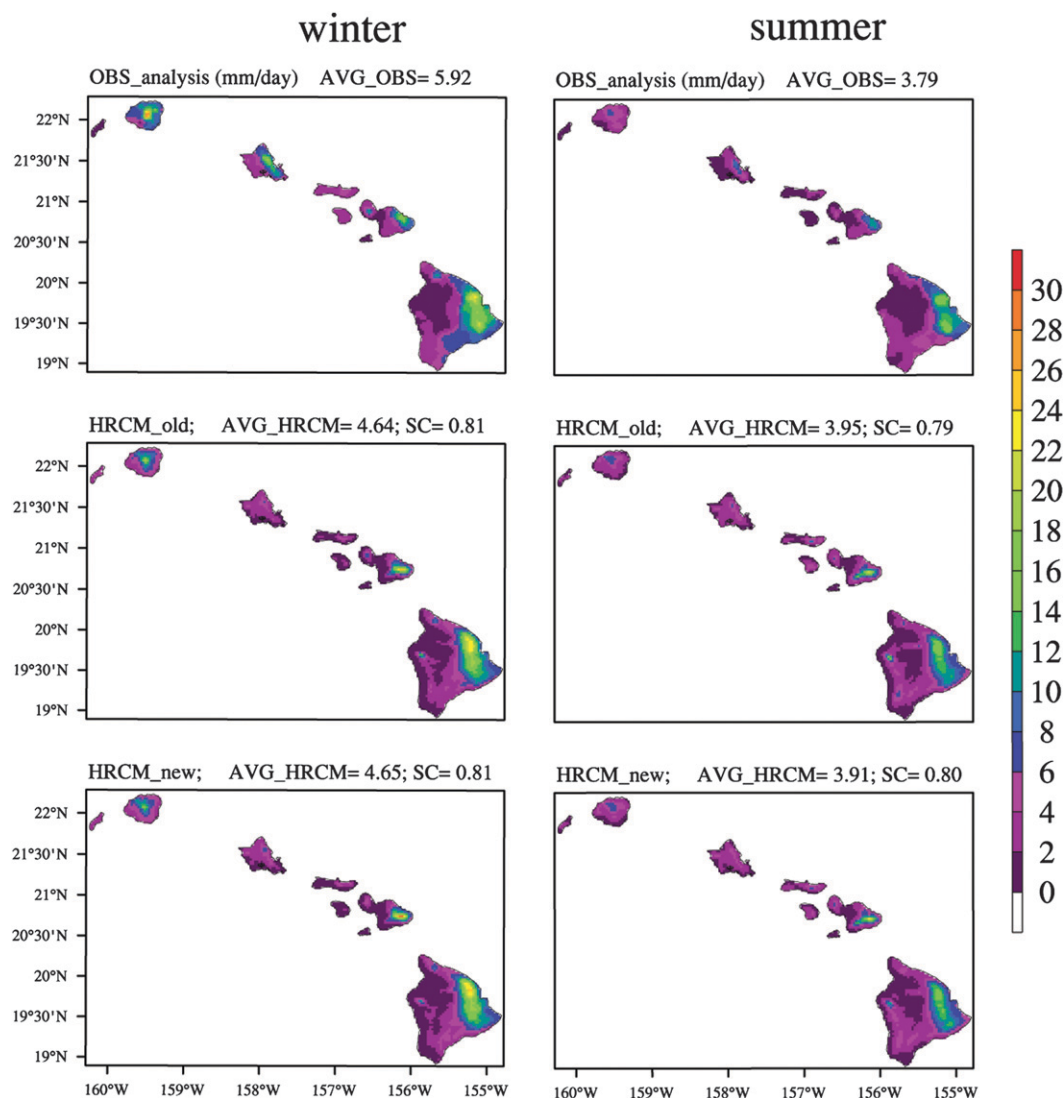


FIG. 10. The observed and the HRCM inner domain simulated seasonal mean precipitation for (left) winter and (right) summer. The numbers above the plots give the domain average for all islands (AVG) and spatial correlation coefficient of model results with observations (SC).

dataset. Similarly to the daily mean values, the model results are not improved at all stations by the new land surface dataset. For instance, the RMSE for T_{\max} at the Kalaeloa airport (PHJR) on Oahu increased from 1.25 to 1.39 K, and T_{\min} increased from 1.53 to 1.93 K. All stations have a cold T_{\max} bias between 0.52 and 2.0 K. Most stations have a warm T_{\min} bias between 0.55 and 1.78 K. Both HRCM simulations have smaller diurnal surface temperature amplitudes than the observations. This is because the simulated T_{\max} is about 1 K lower and the simulated T_{\min} is around 0.7 K higher. The new land surface data do not reduce the bias of the diurnal amplitude of the surface temperature.

2) SPATIAL DISTRIBUTION OF PRECIPITATION

We generated a gridded precipitation dataset for all Hawaiian Islands using the Cressman objective analysis (Cressman 1959) on WRF native grids. The analysis radii are 0.2°, 0.12°, 0.06°, and 0.03° in sequence. The first-guess field is from the Tropical Rainfall Measuring Mission (TRMM-3B43; Huffman et al. 1995). All NCDC, USGS, and Hydronet data are ingested by season. As shown in Fig. 10, the simulations with the old and new land surface datasets both reproduce the observed precipitation well on the windward sides of the islands of Hawaii and of Haleakala on Maui. Both simulations underestimate the precipitation over Oahu in winter,

which is mainly a result of the underestimation of the mean precipitation for all the islands in winter (4.64 and 4.65 mm day^{-1} in the model simulations vs 5.92 mm day^{-1} in the observations). This is because the HRCM simulation does not reproduce the heavy rain events in March 2006 well when a large low pressure system lingered west of the Hawaiian Islands (not shown). Even though this storm is captured by the model, its exact location is not. This clearly shows the challenges of simulating heavy precipitation events by individual storms with a climate model despite the model being forced by observed boundary conditions. The SC of the seasonal mean precipitation is around 0.80. The simulation with the new land surface dataset does not show a higher SC than that with the old land surface dataset.

3) DIURNAL RAINFALL VARIATIONS

The Hydronet rainfall data at 65 observational stations are used to study the diurnal rainfall variations over the Hawaiian Islands for TWI days from 1 November 2005 to 31 October 2006. Here, we use TWI days observed at Lihue, Kauai (PHLI), and Hilo, Hawaii (PHTO). If both stations have a TWI at the same time, we consider it a TWI day, which gives 251 TWI days in the studied period. Note that, the simulated TWI days can differ from the observed ones. We choose TWI days to exclude periods with midlatitude or tropical disturbances (they are discussed separately below) and focus on trade wind regime in the Hawaiian region. The rainfall intensity peak is defined as the hour with the maximum observed hourly rainfall averaged over all TWI days. The rainfall frequency peak is defined as the hour when rainfall occurs most frequently. Because the observational precision is 0.01 in. (0.254 mm), the threshold for recorded rainfall is also 0.254 mm. We normalized the rainfall intensity at each station (the averaged hourly rainfall on all TWI days divided by the daily rainfall amount) before the averaged rainfall intensity was calculated island by island.

Each island has a unique rainfall diurnal cycle (Figs. 11 and 12) and the rainfall intensity peak from the observations shows a large diversity among different islands (Fig. 11a). The island of Kauai has an intensity peak at late night to early morning, while the island of Oahu reaches its intensity peak in the afternoon at most of the observational stations, although the two islands are in close distance and have a similar size. In the northern part of the island of Maui the rainfall intensity peak occurs between midnight and the early morning and in the early afternoon in other parts of Maui. Over the island of Hawaii the rainfall intensity peak occurs in the late afternoon to early night. Over most of the islands the rainfall intensity peak is consistent with the frequency peak or within a few hours at the most except for the

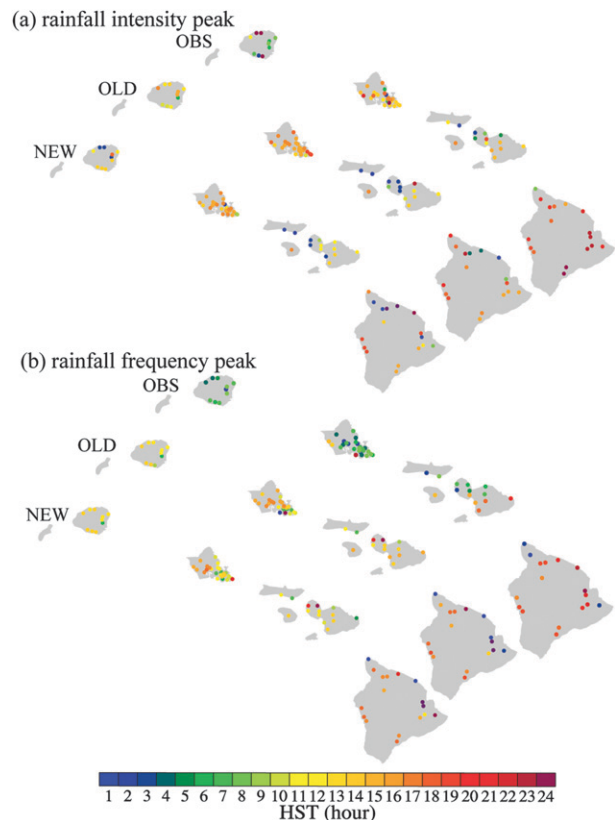


FIG. 11. The observed and the HRCM-simulated (a) rainfall intensity peak and (b) frequency peak. Shown are observations (OBS) and model results using the old land surface dataset (OLD) and using the new land surface dataset (NEW). HST means Hawaiian standard time (UTC - 10 h).

island of Oahu where the intensity peak occurs in the afternoon, while the frequency peak occurs in the early morning (Fig. 11). As can be seen from Fig. 12c, the island of Oahu has two intensity peaks: one is in the early morning and the other is in the early afternoon. The afternoon intensity peak is stronger than the early morning peak, indicating the effects of land heating and terrain on the diurnal precipitation cycle.

The model did not capture the rainfall peak very well for the island of Kauai no matter whether the new or the old land surface dataset was used (Fig. 11). Most stations on Kauai show the peak between midnight and early morning, while the HRCM-simulated rainfall peak occurs in the late morning to midafternoon (Figs. 11 and 12a,b). The observations show an early morning frequency peak over Oahu, while both simulations show the frequency peak in the afternoon at many stations. However, the simulated frequency peak appears in the early morning at some stations in southeast Oahu, consistent with the observations. The two rainfall intensity peaks over the island of Oahu (Fig. 12c) are well reproduced by

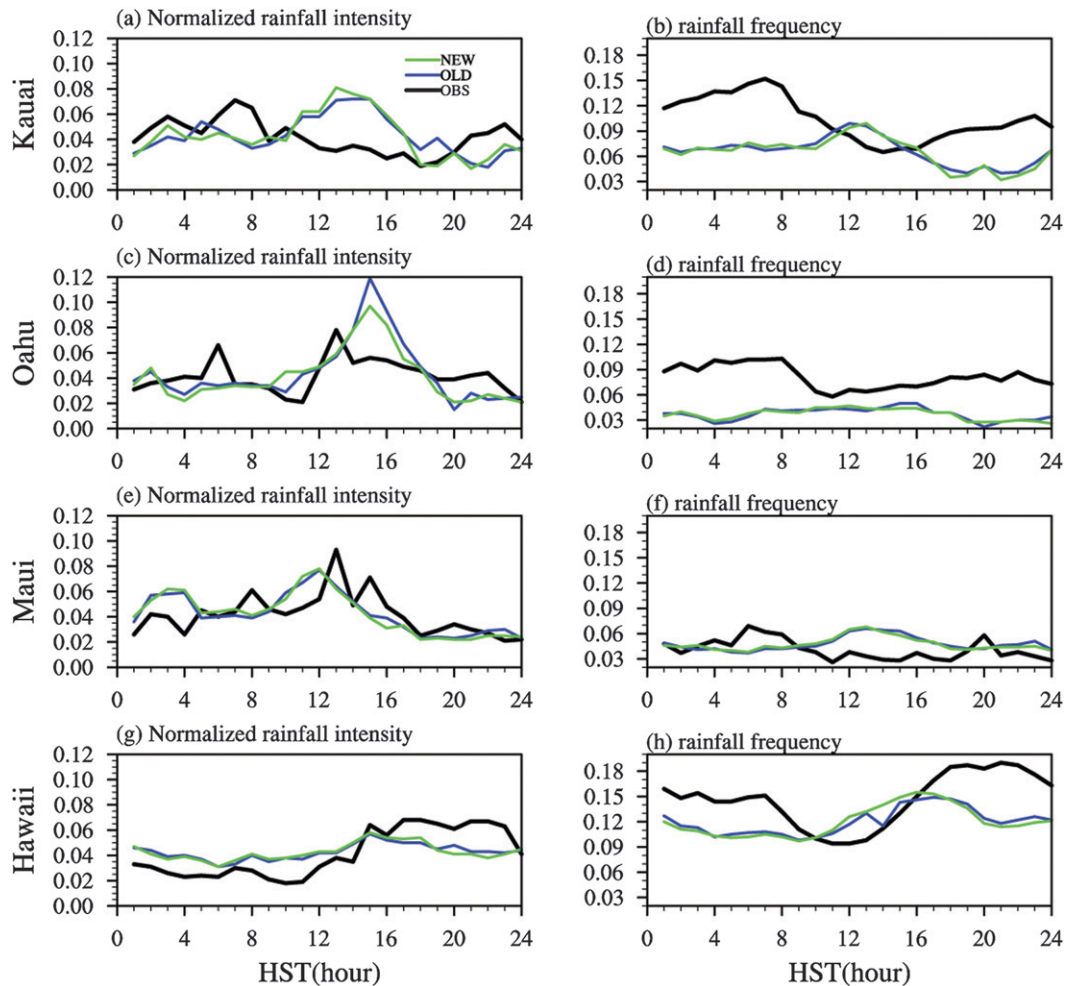


FIG. 12. The normalized diurnal rainfall (a),(c),(e),(g) intensity and (b),(d),(f),(h) frequency averaged over (from top to bottom) Kauai, Oahu, Maui, and Hawaii.

the HRCM, except that the early morning peak is shifted to the middle of the night, and the early afternoon peak is shifted to the midafternoon in the simulations. The simulated rainfall frequencies over the islands of Oahu and Kauai between 0900 and 1600 local time are relatively close to the observations (Figs. 12b,d). The rainfall frequency over these two islands is underestimated at other times in the model simulations. Note that the small variability of the rainfall frequency makes it difficult to estimate the frequency peak accurately. Simulations with the old and the new land surface datasets capture the afternoon rainfall intensity peak over Maui (Figs. 11 and 12e), but both simulations underestimate the rainfall frequency during the daytime. Both simulations also reproduce the rainfall intensity and frequency peaks over the island of Hawaii well (Fig. 11); however, they both underestimate the rainfall intensity at early night and overestimate the rainfall intensity during the day time before 1500 local

time (Figs. 12g,h). Same as on the islands of Kauai and Oahu, the simulations underestimate the rainfall frequency at night on the island of Hawaii. Despite these biases in the simulations, the model shows a clear diurnal precipitation cycle and its variation among different islands.

4) SYNOPTIC VARIABILITY OF PRECIPITATION

An important benchmark for the performance of a regional climate model is its capability to reproduce the synoptic variability. Here we examine the synoptic variation of precipitation based on the pentad mean island-scale precipitation data. We averaged precipitation island by island with the gridded precipitation data as used in the calculation of spatial pattern correlation for the distribution of precipitation. We calculated pentad means for each island from the daily mean precipitation data (Fig. 13). As can be seen from Fig. 13, most heavy rainfall events occurred in the winter of 2006. The

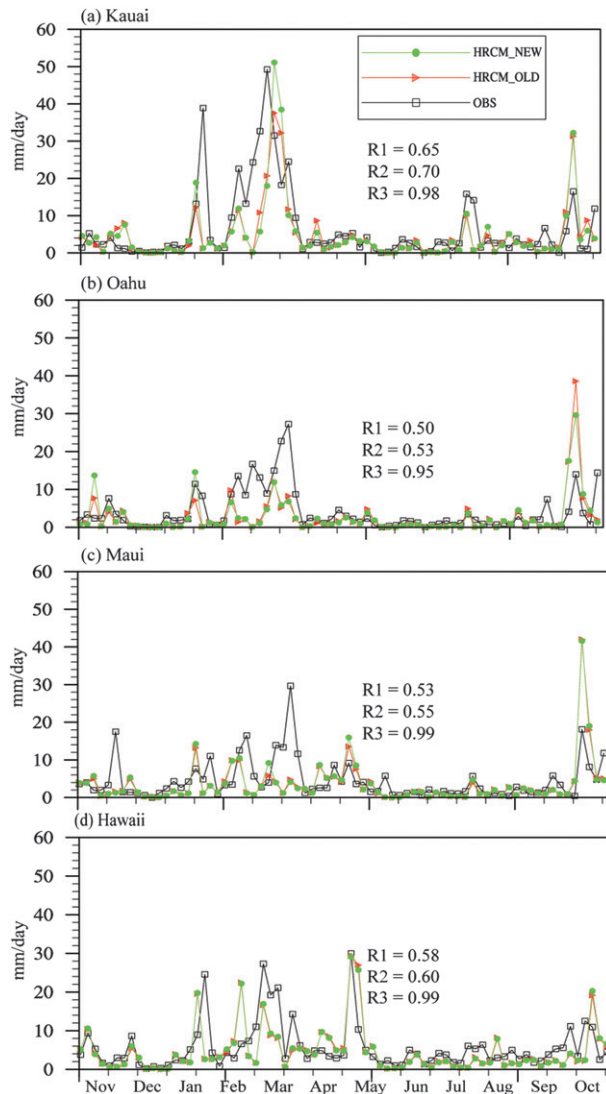


FIG. 13. The time series of the 5-day mean precipitation over the island of (a) Kauai, (b) Oahu, (c) Maui, and (d) Hawaii. OBS means observation, and HRCM_OLD and HRCM_NEW mean the simulations (D2) with old and new land surface data. R1 and R2 mean the correlation coefficients between OBS and HRCM_OLD, OBS and HRCM_NEW, respectively. R3 means the correlation coefficient between HRCM_OLD and HRCM_NEW.

HRCM captures most of the precipitation events reasonably well except for some events in March on the islands of Oahu and Maui. As already discussed above, this is caused mainly by a bias in the location of the simulated storm that was responsible for the heavy precipitation events in March 2006. The storm and the associated frontal systems in the model stayed too far west of Oahu and Maui instead of moving toward the islands as observed. The temporal correlation coefficients reach 0.65, 0.50, 0.53, and 0.58 for Kauai, Oahu, Maui, and Hawaii, respectively, using the new land surface datasets,

which slightly improves the simulation of synoptic variability of precipitation compared to the old land surface dataset. Nevertheless, the relatively high temporal correlation coefficients for the island averages suggest that the model has skills in reproducing the synoptic variability of precipitation in the Hawaiian region.

Figure 14 shows the probability density functions (PDFs) for daily precipitation intensity averaged over the four main Hawaiian Islands from observations and the model simulations with both the new and the old land surface datasets. The simulated rainfall intensity PDFs over the islands of Kauai and Oahu are similar to the observed ones except that the model slightly underestimates light rain over Kauai (Fig. 14a) and overestimates light rain over Oahu (Fig. 14b) and Maui (Fig. 14c). The model slightly underestimates precipitation below 3 mm day^{-1} and slightly overestimates precipitation between $3\text{--}9 \text{ mm day}^{-1}$ for the island of Hawaii. In general, the HRCM tends to simulate slightly more light rain (less than 3 mm day^{-1}) except for the island of Kauai.

4. Summary and conclusions

We have documented the HRCM, which was adapted from the ARW-WRF version 3.3 for climate simulations in the Hawaii region and we evaluated a 1-yr continuous simulation forced by observed lateral boundary conditions. A new land surface dataset based on various data sources was constructed and implemented into the model. This new dataset led to overall improved simulations of surface variables in most of the Hawaiian region compared with the original dataset available with the official release of WRF V3.3. In addition to the new land surface data, we used the Tiedtke convective parameterization scheme in our simulations. The Tiedtke scheme newly implemented into WRF by Zhang et al. (2011) shows superior performance in the Hawaii region with an improved simulation of low-level clouds in the trade wind regime as already shown in Zhang et al. (2011). The parameterizations of the warm rain processes autoconversion and accretion from Khairoutdinov and Kogan (2000) as well as an adjustment of the average cloud droplet number concentration are used to improve the simulations of trade wind cumuli in the Hawaii region.

The results show that the HRCM captured the basic features of the seasonal mean large-scale circulation reasonably well. The seasonal mean MSLP and 500-hPa geopotential height biases are very small, although there are cold and wet biases in the simulated lower troposphere compared to the MERRA reanalysis data. Model results obtained with the new land surface

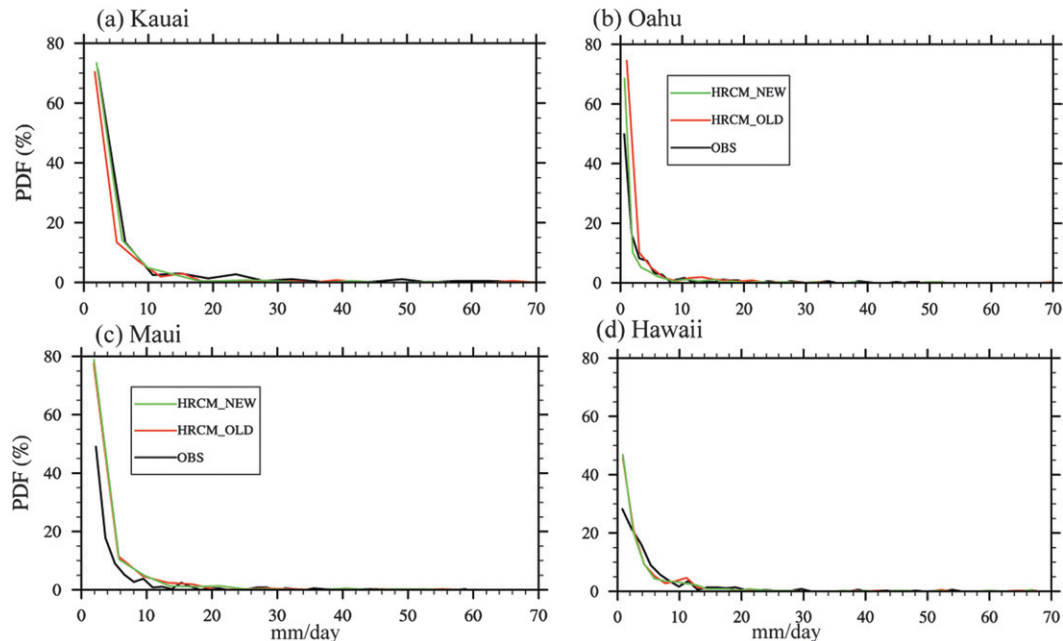


FIG. 14. The daily precipitation PDFs over the island of (a) Kauai, (b) Oahu, (c) Maui, and (d) Hawaii. OBS means observation and HRCM_OLD and HRCM_NEW mean the simulations (D2) with old and new land surface data.

dataset are compared with those obtained with the default land surface dataset provided with the official WRF v3.3 release. In general, the model biases were small for both land surface datasets. The mean daily RMSEs are less than 0.9 K for surface air temperature, less than 7% for surface relative humidity, and less than 2.7 m s^{-1} for surface wind speed over the Hawaiian Islands. The temporal correlation coefficients are 0.85, 0.54, and 0.68 for surface air temperature, relative humidity, and surface wind speed, respectively. The results obtained with the new land surface dataset show an overall improved simulation at most of the stations. However, the new land surface dataset did not improve the simulation of spatial distribution of precipitation. The total precipitation particularly over the windward side of the island of Hawaii and the total cloud fraction in the Hawaiian region are well simulated by the HRCM.

The HRCM captures the main features of the precipitation diurnal cycle in the individual islands reasonably well, such as the double intensity peak over Oahu; however, there are some discrepancies in the model simulations compared with the observations. The HRCM underestimates the rainfall frequencies during the night time over the islands of Oahu, Kauai, and Hawaii. This may be partly due to the limited precision of the observations resulting in a lower threshold of 0.254 mm h^{-1} for the detection of precipitation. This might also explain the overestimation of the light rain frequency by the

model over most of the islands. Since the total precipitation is very close to the observations in summer, the model has systematic bias to simulate more light and less strong rain. The results support earlier findings that precipitation is a particular challenging quantity for dynamical downscaling of climate and climate change in the Hawaii region.

The temporal evolution of the pentad mean precipitation over individual islands was analyzed to examine the model's capability to reproduce the synoptic variability of precipitation in the Hawaiian region. The results show that the HRCM simulates most of the heavy rainfall events reasonably well for all islands although some biases exist. For example, the heavy precipitation event in early March 2006 over island of Kauai was delayed by one pentad while the same event over the islands of Oahu and Maui was missed in the simulation. In general, the simulation with the new land surface dataset shows some improvements compared to the simulation using the original dataset.

This study is the first step toward a comprehensive regional climate model for the Hawaiian Islands. Multi-year continuous simulations are planned for a more systematic evaluation of the model's performance for the region, in particular in reproducing the interannual variability of precipitation associated with the El Niño–Southern Oscillation and any decadal variability in the region potentially related to the Pacific decadal oscillation. These further evaluations are critical to assess the

confidence in dynamical downscaling results with the HRCM of the future climate projections for the Hawaiian Islands.

Acknowledgments. This study was supported by NOAA Grant NA07OAR4310257 and DOE Regional and Global Climate Modeling (RCGM) Program Grant ER64840. Additional support was provided by the Japan Agency for Marine-Earth Science and Technology (JAMSTEC), by NASA through Grant NNX07AG53G, and by NOAA through Grant NA09OAR4320075, which sponsor research at the International Pacific Research Center. We would to acknowledge the Hawaii Open Supercomputer Center for providing access to their facilities.

REFERENCES

- Bukovsky, M. S., and D. J. Karoly, 2009: Precipitation simulations using WRF as a nested regional climate model. *J. Appl. Meteor. Climatol.*, **48**, 2152–2159.
- Cao, G., T. W. Giambelluca, D. E. Stevens, and T. A. Schroeder, 2007: Inversion variability in the Hawaiian trade wind regime. *J. Climate*, **20**, 1145–1160.
- Carlis, D. L., Y.-L. Chen, and V. Morris, 2010: Numerical simulations of island-scale airflow and the Maui vortex during summer trade wind conditions. *Mon. Wea. Rev.*, **138**, 2706–2736.
- Chen, F., and J. Dudhia, 2001: Coupling an advanced land-surface/hydrology model with the Penn State/NCAR MM5 modeling system. Part I: Model description and implementation. *Mon. Wea. Rev.*, **129**, 569–585.
- Chen, Y.-L., and A. J. Nash, 1994: Diurnal variation of surface airflow and rainfall frequencies on the island of Hawaii. *Mon. Wea. Rev.*, **122**, 34–56.
- , and J. Feng, 1995: The influences of inversion height on the precipitation and airflow over the island of Hawaii. *Mon. Wea. Rev.*, **123**, 1660–1676.
- , and —, 2001: Numerical simulations of airflow and cloud distributions over the windward side of the island of Hawaii. Part I: The effects of trade wind inversion. *Mon. Wea. Rev.*, **129**, 1117–1134.
- Chu, P.-S., and J. D. Clark, 1999: Decadal variations of tropical cyclone activity over the central North Pacific. *Bull. Amer. Meteor. Soc.*, **80**, 1875–1881.
- , A. J. Nash, and F. Porter, 1993: Diagnostic studies of two contrasting rainfall episodes in Hawaii: Dry 1981 and wet 1982. *J. Climate*, **6**, 1457–1462.
- Collins, W. D., and Coauthors, 2004: Description of the NCAR Community Atmosphere Model (CAM3.0). NCAR Tech. Note NCAR/TN-464+STR, 226 pp.
- Cressman, G. P., 1959: An operational objective analysis system. *Mon. Wea. Rev.*, **87**, 367–374.
- Csiszar, I., and G. Gutman, 1999: Mapping global land surface albedo from NOAA AVHRR. *J. Geophys. Res.*, **104** (D6), 6215–6228.
- Dee, D. P., and Coauthors, 2011: The ERA-Interim reanalysis: Configuration and performance of the data assimilation system. *Quart. J. Roy. Meteor. Soc.*, **137**, 553–597.
- Esteban, M. A., and Y. L. Chen, 2008: The impact of trade wind strength on precipitation over the windward side of the island of Hawaii. *Mon. Wea. Rev.*, **136**, 913–928.
- Feng, J., and Y. L. Chen, 2001: Numerical simulations of airflow and cloud distributions over the windward side of the island of Hawaii. Part II: Nocturnal flow regime. *Mon. Wea. Rev.*, **129**, 1135–1147.
- Giambelluca, T. W., and M. A. Schroeder, 1986: *Rainfall Atlas of Hawaii*. Rep. R76, Department of Land and Natural Resources Hawaii, 267 pp.
- Guo, P., Y.-H. Kuo, S. V. Sokolovskiy, and D. H. Lenschow, 2011: Estimating atmospheric boundary layer depth using COSMIC radio occultation data. *J. Atmos. Sci.*, **68**, 1703–1713.
- Gutman, G., and A. Ignatov, 1998: The derivation of green vegetation fraction from NOAA/AVHRR data for use in numerical weather prediction models. *Int. J. Remote Sens.*, **19**, 1533–1543.
- Homer, C., C. Huang, L. Yang, B. Wylie, and M. Coan, 2004: Development of a 2001 National Land-Cover Database for the United States. *Photogramm. Eng. Remote Sens.*, **70**, 829–840.
- Hong, S.-Y., and J. Lim, 2006: The WRF single-moment 6-class microphysics scheme (WSM6). *J. Korean Meteor. Soc.*, **42**, 129–151.
- Huffman, G. J., R. F. Adler, B. Rudolf, U. Schneider, and P. R. Keehn, 1995: Global precipitation estimates based on a technique for combining satellite-based estimates, rain gauge analysis, and NWP model precipitation information. *J. Climate*, **8**, 1284–1295.
- Janjić, Z. I., 1996: The surface layer in the NCEP Eta Model. Preprints, *11th Conf. on Numerical Weather Prediction*, Norfolk, VA, Amer. Meteor. Soc., 354–355.
- , 2002: Nonsingular implementation of the Mellor–Yamada level 2.5 scheme in the NCEP Meso model. NCEP Office Note 437, 61 pp.
- Jiménez, P. A., J. Fidel González-Rouco, E. García-Bustamante, J. Navarro, J. P. Montávez, J. Vilà-Guerau de Arellano, J. Dudhia, and A. Muñoz-Roldan, 2010: Surface wind regionalization over complex terrain: Evaluation and analysis of a high-resolution WRF simulation. *J. Appl. Meteor. Climatol.*, **49**, 268–287.
- Khairoutdinov, M., and Y. Kogan, 2000: A new cloud physics parameterization in a large-eddy simulation model of marine stratocumulus. *Mon. Wea. Rev.*, **128**, 229–243.
- Leung, L. R., Y. H. Kuo, and J. Tribbia, 2006: Research needs and directions of regional climate modeling using WRF and CCSM. *Bull. Amer. Meteor. Soc.*, **87**, 1747–1751.
- Lyons, S. W., 1982: Empirical orthogonal function analysis of Hawaiian rainfall. *J. Appl. Meteor.*, **21**, 1713–1729.
- Nguyen, H. V., Y. L. Chen, and F. Fujioka, 2010: Numerical simulations of island effects on airflow and weather during the summer over the island of Oahu. *Mon. Wea. Rev.*, **138**, 2253–2280.
- Otkin, J. A., and J. E. Martin, 2004: A synoptic climatology of the subtropical Kona storm. *Mon. Wea. Rev.*, **132**, 1502–1517.
- Pincus, R., S. Platnick, S. A. Ackerman, R. S. Hemler, and R. J. P. Hofmann, 2012: Reconciling simulated and observed views of clouds: MODIS, ISCCP, and the limits of instrument simulators. *J. Climate*, **25**, 4699–4720.
- Reynolds, R. W., C. L. Gentemann, and G. K. Corlett, 2010: Evaluation of AATSR and TMI satellite SST data. *J. Climate*, **23**, 152–165.
- Rienecker, M. M., and Coauthors, 2011: MERRA: NASA's Modern-Era Retrospective Analysis for Research and Applications. *J. Climate*, **24**, 3624–3648.

- Rummukainen, M., 2010: State-of-the-art with regional climate models. *Climate Change*, **1**, 82–96.
- Schaaf, C. B., and Coauthors, 2002: First operational BRDF, albedo nadir reflectance products from MODIS. *Remote Sens. Environ.*, **83**, 135–148.
- Schroeder, T. A., 1981: Characteristics of local winds in Northwest Hawaii. *J. Appl. Meteor.*, **20**, 874–881.
- , 1993: Climate controls. *Prevailing Trade Winds: Weather and Climate in Hawai'i*, M. Sanderson, Ed., University of Hawai'i Press, 12–36.
- , B. J. Kilonsky, and B. N. Meisner, 1977: Diurnal variation in rainfall and cloudiness. VH-MET 77-03, Dept. of Meteorology, University of Hawaii at Manoa, 67 pp. [Available from Dept. of Meteorology, University of Hawaii at Manoa, 2525 Correa Rd., Honolulu, HI 96822.]
- Skamarock, W. C., J. B. Klemp, J. Dudhia, D. O. Gill, D. M. Barker, W. Wang, and J. G. Powers, 2008: A description of the Advanced Research WRF Version 3. NCAR Tech. Note 475+STR, 113 pp.
- Tripoli, G. J., and W. R. Cotton, 1980: A numerical investigation of several factors contributing to the observed variable intensity of deep convection over south Florida. *J. Appl. Meteor.*, **19**, 1037–1063.
- Wang, Y., O. L. Sen, and B. Wang, 2003: A highly resolved regional climate model (IPRC_RegCM) and its simulation of the 1998 severe precipitation events over China. Part I: Model description and verification of simulation. *J. Climate*, **16**, 1721–1738.
- , S.-P. Xie, H. Xu, and B. Wang, 2004: Regional model simulations of marine boundary layer clouds over the Southeast Pacific off South America. Part I: Control experiment. *Mon. Wea. Rev.*, **132**, 274–296.
- Wyant, M. C., and Coauthors, 2009: The PreVOCA experiment: Modeling the lower troposphere in the Southeast Pacific. *Atmos. Chem. Phys.*, **9**, 23 909–23 953, doi:10.5194/acpd-9-23909-2009.
- Xu, K.-M., and D. A. Randall, 1996: A semiempirical cloudiness parameterization for use in climate models. *J. Atmos. Sci.*, **53**, 3084–3102.
- Yang, Y., Y.-L. Chen, and F. M. Fujioka, 2005: Numerical simulations of the island-induced circulation over the island of Hawaii during HaRP. *Mon. Wea. Rev.*, **133**, 3693–3713.
- Zeng, X., and A. Beljaars, 2005: A prognostic scheme of sea surface skin temperature for modeling and data assimilation. *Geophys. Res. Lett.*, **32**, L14605, doi:10.1029/2005GL023030.
- Zhang, C.-X., Y. Wang, and K. Hamilton, 2011: Improved representation of boundary layer clouds over the Southeast Pacific in WRF-ARW using a modified Tiedtke cumulus parameterization scheme. *Mon. Wea. Rev.*, **139**, 3489–3513.
- Zhang, Y., Y.-L. Chen, S.-Y. Hong, H.-M. H. Juang, and K. Kodama, 2005a: Validation of the coupled NCEP Mesoscale Spectral Model and an advanced land surface model over the Hawaiian Islands. Part I: Summer trade wind conditions and a heavy rainfall event. *Wea. Forecasting*, **20**, 847–872.
- , —, and K. Kodama, 2005b: Validation of the coupled NCEP Mesoscale Spectral Model and an advanced land surface model over the Hawaiian Islands. Part II: A high wind event. *Wea. Forecasting*, **20**, 873–895.
- , V. Dulière, P. W. Mote, and E. P. Salathé, 2009: Evaluation of WRF and HadRM mesoscale climate simulations over the U.S. Pacific Northwest. *J. Climate*, **22**, 5511–5526.